Stability of and conduction in single-walled Si_2BN nanotubes

Deobrat Singh [1,*,†] Vivekanand Shukla [2,*,‡] Nabil Khossossi [1] Per Hyldgaard [2] and Rajeev Ahuja [1,3]

[1]*Condensed Matter Theory Group, Materials Theory Division, Department of Physics and Astronomy, Uppsala University, Box 516, 75120 Uppsala, Sweden*

[2]*Department of Microtechnology and Nanoscience-MC2, Chalmers University of Technology, SE-41296, Gothenburg, Sweden*

[3]*Department of Physics, Indian Institute of Technology Ropar, Rupnagar 140001, Punjab, India*

(Received 1 June 2022; revised 1 September 2022; accepted 7 October 2022; published 2 November 2022)

We explore the possibility and potential benefit of rolling a Si_2BN sheet into single-walled nanotubes (NTs). Using density functional theory (DFT), we consider both structural stability and the impact on the nature of chemical bonding and conduction. The structure is similar to carbon NTs and hexagonal boron-nitride (hBN) NTs and we consider both armchair and zigzag Si_2BN configurations with varying diameters. The stability of these Si_2BN NTs is confirmed by first-principles molecular dynamics calculations, by exothermal formation, an absence of imaginary modes in the phonon spectra. Also, we find the nature of conduction varies from semiconducting over semimetallic to metallic, reflecting differences in armchair/zigzag-type structures, curvature effects, and the effect of quantum confinement. We present a detailed characterization of how these properties lead to differences in both the bonding nature and electronic structures.

DOI: 10.1103/PhysRevMaterials.6.116001

I. INTRODUCTION

Low dimensional material research has produced exciting results by combining computational predictions, experimental synthesis, and characterization [1]. The immense interest in low dimensional materials is fueled by alluring properties and a broad range of potential applications, such as quantum computing, batteries, electrocatalysis, photovoltaics, electronics, biomedicals, and photonics [2–8]. There exists a broad range of two-dimensional (2D), one-dimensional (1D), and even dotlike structures. These new materials have unique properties and functionalities that are hard to achieve in their three-dimensional counterparts [9,10].

Computer-assisted materials design today supplements and strengthens the traditional Edisonian-laboratory type exploration. The latter rely on constructive feedback between synthesis and characterization in a trial and error process, and it must, of course, eventually be pursued as we seek progress on functionality. However, the use of first-principle density functional theory (DFT) allows us to first make reliable predictions of properties, ahead of synthesis. We can therefore focus the more labor-intensive wet-lab activity on the most promising materials.

There is also good reason to use predictive theory to both screen for likely strong performers and to also explore the result database for beneficial material transformations (into lower-dimensional forms). It is, for example, possible to roll up a 2D sheet into a single-walled nanotube (NT), e.g., graphene (or hexagonal boron-nitride) into carbon (or hBN) NTs. Excitingly, theory results for the 2D form may here provide insight on properties of the NT form [11] and give us ideas to rig this transformation to control the resulting NT electronic structure. There are a number of material-theory predictions that were later successfully realized in experiments giving trust in the use of a material-prediction database. Similarly, the idea of mapping for structure-transformation benefits is today considered a standard option for a further tuning of the structural and electronic properties [12,13]. There has been number of nanomaterials predicted before their experimental synthesis. 2D Borons, boron carbon nitride, graphitic carbon nitride, silicon carbon nitride polymorphs, Janus transition metal chalcogenides, and very recently various 2D magnetic materials were synthesized after the predictions with high level of theory both in layered and NT forms [14–25]. Furthermore, these nanomaterials have been explored in variety of electrochemical, sensing and optoelectronic applications [26–43].

The Si_2BN is a particular 2D system that is currently attracting significant attention even if it has not yet been synthesized. The theoretical predictions of Si_2BN nanosheets go for planar structure [44–46], having Si-Si-B-N arrangement similar to graphene. Si_2BN sheets are predicted to show dynamic (phonon) and elevated-temperature stability as demonstrated in the *ab initio* and molecular dynamics studies. They are also predicted to have a high cohesive energy similar to graphene and h-BN monolayer. Realization of this sheet is a motivation for experimetalists, noting that it was predictions

*These authors contributed equally to this article.
†deobrat.singh@physics.uu.se
‡vivekanand.shukla@chalmers.se

of 2D boron, graphane, BC_2N and several other 2D sheets that led to experimental realization [47,48].

Considering theory predictions of a strong stability of the Si_2BN sheet and considering the potential of the applications, it is also natural to next inquire whether there are also benefits in rolling Si_2BN into a 1D NT form?

In this paper, we propose to explore potential benefits of such Si_2BN transformations. To that end, we map the structure and electronic-structure impact of various forms of sheet rollings. A key motivating factor is that Si_2BN systems presents us with a richer chemistry and therefore also a richer physics of the corresponding 1D form, compared to graphene and carbon NTs. The Si atom has Si, B, and N as nearest neighbors, while each B (N) has two Si atoms and one N (B) atom as nearest neighbors. The Si atoms find themselves in electron-deficient position and the variation in bonds works as an electron reservoir for an adatom or a molecule on the sheet (or NT) surface. There have been a number of computational studies, that explored the potential of 2D Si_2BN for various applications such as hydrogen storage [49,50], metal-ion batteries [51], gas sensing [52], active catalyst for hydrogen evolution reactions [53] in the short span of time that has passed since the first theoretical prediction of Si_2BN sheets. Theory suggests that the electronic structure of 2D Si_2BN is metallic [54], whereas, a semiconducting nature of conductions is desired for various potential applications [55,56].

Fortunately, Si_2BN presents intriguing possibilities for rolling into NT conformations and thereby control the nature of conduction. This control goes beyond what is possible in the carbon and hBN NT counterparts [11]. Interestingly, the hexagons in Si_2BN planer structures are distorted in shape (unlike graphene and silicene) owing to variations in the electronegativity and in the covalent radii. This, in turn, implies the presence of strain, although we are still staying close to the sp^2-hybridized chemical bonding that characterize graphene.

Mintmire *et al.* showed that the orientation of the rolling (NT) axis (relative to the graphene hexagons) determines whether we get a metallic or semiconducting carbon NT, in a universal relationship [11] (that applies without pronounced rehybridization). The Si_2BN sheet does not show a Dirac-cone behavior at the Fermi level, but the resulting NTs possibly can retain a sharp density of state around the Fermi level [44,51]. On the one hand, we can therefore expect the general ideas to guide us [11]. On the other hand, unlike for carbon NTs, we can now also adjust the extent that we let the Si-atom site carry the main load of rolling-induced strain. This fact provides us with additional options to control the electronic structure details in the Si_2BN NTs.

We use first-principles DFT calculations and transport studies to demonstrate that the rolling of Si_2BN sheet into a NT geometry is indeed possible (in terms of structural stability) and allows control of the nature of conduction. In fact, motivated by the potential for a richer band gap engineering, we systematically investigate the electronic properties and bonding characteristics of a range of single-walled Si_2BN NTs of various sizes and choice of rolling axis. For two main options for Si_2BN rolling (corresponding to armchir and zigzag rolling of carbon NTs), we validate the mechanical stability by documenting an absence of vibrational instabilities and by tracking the systems using Ab Initio molecular dynamics. More broadly we use a crystal-orbital Hamiltonian population (COHP) analysis to document that the bonding between the Si-Si, Sb-B/N, and B-N atoms retains a pronounced covalent nature; A special case is discussed in Ref. [57]. We take the COHP characterization as an indicator that the new NTs are stable. We also take this information as a sign that the Si_2BN NTs will resist (as do carbon NTs) forming strong chemical bonds in connection with functionalization and doping. We generally expect that the interaction with the environment will occur through weak chemisorption [58–64].

This paper is organized as follows. The following section, Sec. II, describes the theoretical approaches. The results and discussion section, Sec. III, is separated into three main themes. Section III A reports our predictions of the resulting NT structures and discusses the mechanical and chemical stability, Sec. III B reports our exploration of the electronic properties, while Sec. III B presents and discusses the results of our chemical-bond analysis. We conclude the results and outcome in conclusions section, Sec. IV.

II. COMPUTATIONAL METHOD

First-principles calculations are employed with the plane-wave basis projector augmented wave (PAW) method in the framework of density-functional theory (DFT) [65] coded in Vienna *ab initio* simulation package (VASP) software [66] version 5.4. For the exchange-correlation potential, we use the generalized gradient approximation (GGA) in the form of the Perdew-Burke-Ernzerhof (PBE) functional [67]. The energetics of rolling of a sheet ribbon into a NT involves balancing a large exothermal process of sealing the ribbon edges against significant cost of mechanical deformations. We ignore long-range dispersion effects, for example, as described in the vdW-DF method [64,68] since we expect that both of these competing energies are primarily defined by the presence of strong covalent bonds in the Si_2BN material.

A plane-wave basis-set energy cutoff value is first converged and then taken to be 500 eV throughout our calculations, including first-principle molecular dynamics simulations. These calculations were performed using the scalar relativistic PAW pseudopotentials (PPs) considering Si ($1s^2$, $2s^2$, $2p^6$), B ($1s^2$), and N ($1s^2$) atoms as core electrons, which therefore had 5, 3, and 5 valence electrons, respectively. The total energy was minimized until the energy variation in successive steps became less than 10^{-6} eV in the structural relaxation and the convergence criterion for the Hellmann-Feynman forces was taken to be 10^{-3} eV/Å. We utilized the $24 \times 1 \times 1$ Γ-centred k-point sampling for the unit cell in single-walled Si_2BN NTs for the electronic structure. The density of states (DOS) was plotted with 0.026 eV Gaussian broadening (to allow us to easily interpret predictions for the room-temperature nature of conduction). We studied the NT in unit cells and supercells in which we have added a 15 Å vacuum spacing in the lateral dimensions to minimize the spurious interaction between the periodically repeated NT images.

The charge transfers in different elements in the NTs structures were determined by the postprocessing tool Bader analysis [69] implemented in VASP. The first-principles

molecular dynamics (FPMD) was applied to check the thermal stability at high temperatures. The canonical (fixed number of atoms N, fixed volume V, and a fixed temperature T) NVT ensemble was used during FPMD simulation for 5 ps with the time steps of 2 femtoseconds (fs) and the temperature was controlled via Nosé-Hoover method [70]. We used the PHONOPY code to calculate the phonon dispersion spectra computed via density functional perturbation theory (DFPT) [71]. We calculated the crystal orbital Hamiltonian population (COHP) using the Local orbital basis suite towards electronic-structure reconstruction (LOBSTER) software package [72].

Finally, the electronic transport calculations were performed using the non-equilibrium Green function (NEGF) formalism, ignoring inelastic and dephasing scattering events. Here we used the quantum transport code TRACSIESTA that is implemented along with localized atomic orbital basis set code SIESTA [73,74]. We used same PBE exchange-correlation functional in our transport calculations with the Troullier-Martins [75] norm-conserving PPs considering 5, 3, and 5 valence electrons for Si, B, and N atoms, respectively. A mesh cutoff of 250 Ry was used for real-space integration, and for Brillouin-zone sampling, $24 \times 1 \times 1$ mesh was considered. Our structural relaxation tests suggested that there was small deviation in Si-Si, Si-B, Si-N, and B-N bond lengths in relaxed geometry with SIESTA code as compared to VASP results, a detailed information is given in table S1 in SM [57]. Therefore we used a fix geometry calculated in plane wave for our electronic transport calculations.

III. RESULTS AND DISCUSSION

A. Structural characterization and stability

The single-walled Si_2BN NTs are formed from a ribbon of graphene-like Si_2BN monolayer. The monolayer ribbon is rolled up into a hollow seamless cylinder in a similar way as carbon NTs [11] and Type-I BC_2N NTs can be rolled [76]. To provide a simple nomenclature, we use $\mathbf{a}_{1,2}$ to denote the unit vectors for the hexagonal structure in the sheet and assume that the NT arises as a mathematical construction. First starting with any atom, we consider a so-called chiral vector

$$C_h = n\mathbf{a}_1 + m\mathbf{a}_2, \tag{1}$$

that will take us to another equivalent atom in the sheet (taking m and n directions of the basis vectors). We next assume that we make a ribbon by cutting the sheet at right angles at the start and just before the very end of this vector; These edges define the resulting NT axis. Finally, we see the NT conformation as resulting after bending the ribbon and rebonding at the edges. Equation (1) is also called the roll-up vector since it connects repeated ribbon images of the sheets and therefore defines the atomic structure in the circumference of the resulting cylinder.

Figure 1(a) identifies the chiral angle θ that the roll-up or chiral vector has with the hexagonal-sheet basis vectors. The panel also illustrates two main cases, "zigzag" NTs that corresponds to $\theta = 0$ and "armchair" NTs that corresponds to $\theta = 30$. For these NT constructions, one must use ribbons with a chiral vector set by $(n, 0)$ and $(n, m = n)$ in-sheet steps, respectively. Figure 1(b) shows the schematic of resulting

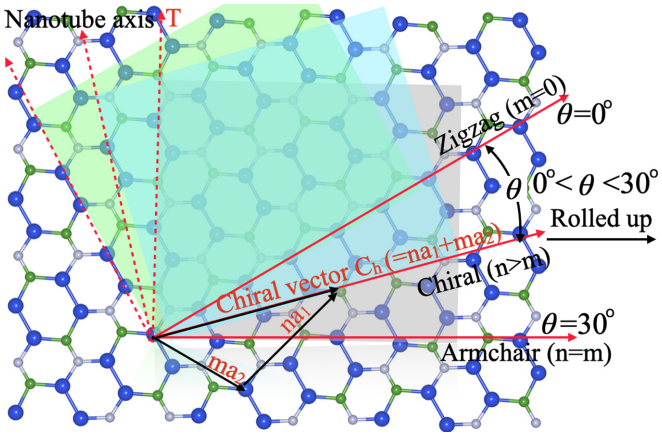

FIG. 1. Schematics of a planar, hexagonal-type Si_2BN nanosheet and of possibilities for rolling-up conformational changes (identified by a chiral vector) that leads to NT forms. The sheet starting point is distorted (relative to the ideal hexagonal pattern) due to the in-plane variation in atomic composition and the nature of chemical bonds. An angle Θ of the chiral vector controls the direction of the axis of the rolled-up NT and illustrates choices that lead to both armchair, zigzag, and general 1D Si_2BN forms.

zigzag and armchair Si_2BN NTs that both approximately have a 1.5 nm diameter.

Importantly, Fig. 1(a) also clarifies that Si_2BN have fewer possibilities for rolling into a NT (compared with graphene). This is because the sheet is a triple-element system and we we must have periodicity as we revolve around the cylinder. A chiral vector cannot start with a Si atom and end with a B or N atom. Nevertheless we have constructed and characterized a total of five zigzag NTs and seven armchair NTs of various diameters.

Figures 2(a) and 2(b) shows our computed results for the fully relaxed structures of two moderately large Si_2BN NTs. We contrast a zigzag and an armchair forms, top and bottom set of panels, respectively. In both cases, we aimed to have approximately a 1.5 nm diameter, and therefore considered the armchair (4,4) and zigzag (7,0) NTs for detailed stability analysis, below.

The zigzag and armchair Si_2BN NTs have 64 (32-Si, 16-B, and 16-N) and 112 (56-Si, 28-B, and 28-N) atoms in the unit cell, respectively. The unit cell lengths along the axial directions are 6.45 and 11.06 Å for the armchair and zigzag directions, respectively. We use an initial structure guess to start a DFT study of the atomic relaxation in both NT case, and find that the curvatures influence the bond lengths slightly. The fully relaxed NT bond lengths are Si-Si (2.24 Å), Si-B (1.96 Å), Si-N (1.77 Å), and B-N (1.46 Å), that is, very similar to those that characterize the 2D Si_2BN monolayer form (2.246, 1.951, 1.756, and 1.466 Å) [53].

To further probe the energetic stability of the fully relaxed NTs, we calculated the cohesive energies and compared them with various other well studied NTs.

$$E_{\text{coh}} = E_{\text{NT}} - E_{\text{Si}} - E_{\text{B}} - E_{\text{N}}, \tag{2}$$

Here E_{NT} is the energy of the NTs and E_{Si}, E_{B}, and E_{N} are the energies of the isolated Si, B, and N atoms, respectively. Our NTs cohesive energy results may depend weakly on the choice

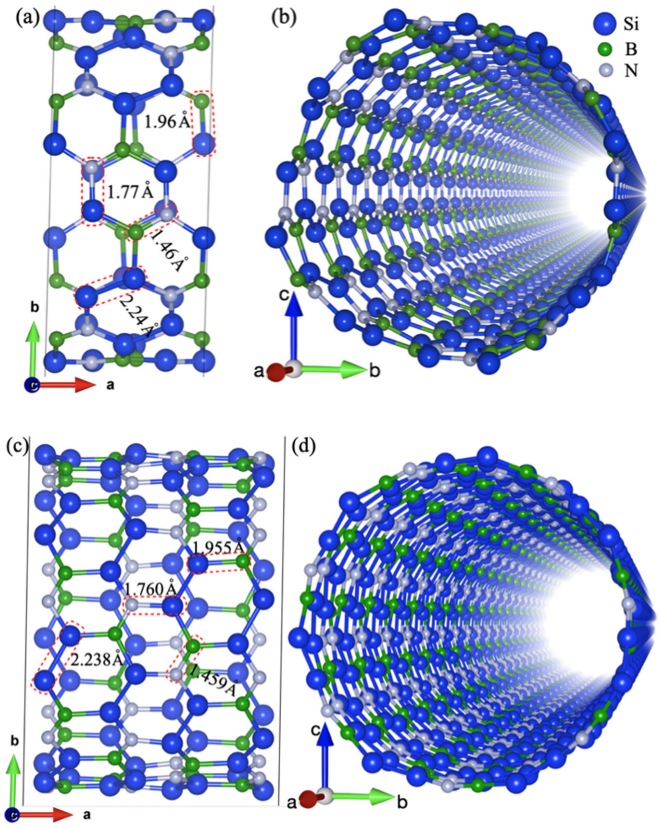

FIG. 2. Optimized structures of [(a) and (b)] armchair (4,4) and [(c) and (d)] zigzag (7,0) Si_2BN nanotube with top view and other orientation. The blue, green and light gray color represent the Si, B, and N atoms, respectively. The bond lengths in fully relaxed ground state structures are indicated in respective figures.

of pseudopotentials that we use for the DFT calculations. Table I shows the cohesive energies of Si_2BN NT geometries compared with the available literature values for various other NT geometries. Armchair and zigzag Si_2BN NTs cohesive energies (4.92 and 4.90 eV, respectively) suggest that these are stable compared to silicon, boron, and phosphorus-based NTs. Si_2BN NTs are predicted to be less stable than C and hBN NTs, but more stable than Si NTs. We still expect metastability because (as we document in the following section) all bonds retains a pronounced covalent character, implying that there are dramatic costs in breaking any of the Si_2BN bonds.

TABLE I. Cohesive energies (in eV/atoms) of single-walled Si_2BN NTs in armchair (4,4) and zigzag (7,0) forms. Atomic reference energies for Si, B and N are calculated using spin polarized calculations (using unit-cell sizes with 15 Å vacuum spacing between the repeated images of the NTs). These cohesive energies of Si_2BN nanotubes are compared with available cohesive energies for various other nanotubes in the literature.

System	E_{coh}	Ref.
Borophene	3.44	[77]
Silicene	4.01	[78]
Blue phosphorene	4.41	[79]
Graphene	7.90, 8.72	[80–82]
Graphyne	7.02	[83]
Boron nitride	7.59	[82]
Si_2BN nanotube zigzag/armchair	4.92/4.90	This work

To further confirm the energetic stability of Si_2BN NTs, we also investigate the impact of increasing the NT diameters to ∼2.5 nm, in the armchair (7,7) and the zigzag (12,0) NTs. We find that the cohesive energy remains unchanged (4.89 and 4.91 eV/atom for the larger armchair and zigzag Si_2BN NTs, respectively). Additionally, we characterize the cohesion and stability of the smallest possible diameter NTs, performing both DFT relaxation studies and a complete phonon characterization for the armchair (1,1) and zigzag (2,0) NTs. A detailed description of those test can be found in Ref. [57]. There is eventually a dynamical instability, but these small-NT studies also help document that the Si_2BN NTs retain mechanical stability over a broad range of diameters.

Table II tracks our predictions for strain energies and for band gaps for both the armchair and zigzag NT geometries across the varying diameters. The strain energy

$$E_{\text{strain}} = E_{\text{sheet/atom}} - E_{\text{NT/atom}} \tag{3}$$

is calculated by subtracting the NT's energy per atom ($E_{\text{NT/atom}}$) with the per-atom energy ($E_{\text{sheet/atom}}$) of Si_2BN in planner form. We find that the strain energy decreases with the diameter, and as expected, a higher stability of larger NTs. A decreasing impact of strain also manifests itself when we track the length of Si-Si, Si-B, Si-N, and B-N bonds in the NTs. Table III clearly shows that bonds are strained in low diameter tubes, and this strain does eventually cause a dynamical instability, see Ref. [57].

Figure 3 shows the phonon dispersion band structure for the armchair (4,4) nanotube that has a ∼1.5 nm diameter. We find no imaginary phonon modes in the spectra, thus documenting also dynamical stability of this NT. A similar conclusion holds for the zigzag NTs of similar diameters.

The phonon characterizations also allow us to discuss thermodynamic properties. We focus on the free energy, the specific heat at constant volume C_V [84–86], and the vibrational entropy. Figure S2 in Ref. [57] presents our DFT-based predictions for those properties as a function of the temperature.

We find that the (armchair) NT free energy decreases monotonically with increasing temperature, whereas vibrational entropy tends to increase. The heat capacity C_V increases very rapidly at low temperatures, reflecting an expected compliance with the Debye law (T^3) [87], At temperatures above 600 K, the C_V rolls over to a constant, hence also complying with the Dulong-Petit law [88].

Our access to the predicted phonon density of states, Fig. S2 of Ref. [57], also allows us to provide a simple discussion of the vibrational contribution to the low-dimensional thermal conductivity [89–97]. The lattice part of the NT thermal conductivity is itself proportional to the heat capacity C_V [98] and to the expected mean-free phonon path. The latter reflect a "wire" scattering time [89,96] and the relevant (along-axis) phonon group velocity that involves a projection of the density of state [91,93,99] (along the NT axis). For low-dimensional systems it is not, in general, easy to extract

TABLE II. Comparison of a chiral vector (n, m), diameters in nanometer (nm) and the number of atoms in the unit-cell during calculation for various Si_2BN armchair (ac) and zigzag (zz) NTs. We also list computed values for the strain energy E_{strain} and the nature of conduction and compares the semiconductor band gap E_g (when present).

acSi_2BN nanotube	No. of atoms	NT diameter (nm)	E_{strain} (eV/atom)	E_g (eV)
(1,1)	16	~0.4	0.184	Metallic
(2,2)	32	0.7	0.086	0.09 (Indirect)
(3,3)	48	1.06	0.050	Semimetallic
(4,4)	64	1.5	0.033	Metallic
(7,7)	112	2.5	0.045	Metallic
zzSi_2BN nanotube	No. of atoms	diameter (nm)	E_{strain} (eV/atom)	Eg (eV)
(2,0)	32	~0.4	0.117	0.11 (Direct)
(3,0)	48	0.61	0.078	0.14 (Indirect)
(4,0)	64	0.82	0.066	0.05 (Indirect)
(5,0)	80	1.03	0.054	0.18 (Indirect)
(6,0)	96	1.23	0.041	Semimetallic
(7,0)	112	1.5	0.032	Semimetallic
(12,0)	192	2.5	0.026	Metallic

this information from density of state but we can proceed as follows.

First, we observe that the heat capacity is significantly higher for the Si_2BN NT than in C NT s [84,100,101]. This itself suggest a high lattice thermal conductivity.

Next, we consider a DFT-based evaluation of the bonding stiffness for the Si_2BN NT. We provide a spring-constant analysis from our calculations of the harmonic-force-constant tensor that describe coupling between nearest-neighbor atom pairs [102,103]. The spring constants, in this case, are 12.57, 17.15, 13.16, and 26.54 eV/Å for atom pairs Si-Si, Si-N, Si-B, and B-N, respectively. These values are higher than the values that applies for most of the materials that have previously been explored [104–106]. The large Si_2BN NT spring-constant values (reflecting stiff bonds) explains the large predicted value for the high-temperature Dulong-Petit C_V limit (and equivalently, a large acoustic-cutoff frequency $\omega_{cut} = 360$ cm^{-1}, indicated by a dotted line in Fig. S2 and by the plotting range in Fig. 3). The large C_V value will itself impact the Si_2BN NT thermal conductivity.

Meanwhile, the NT phonon group velocity is set by the ratio of the spring constants and the masses, see for example, Refs. [91,97]. The weighted impact of such phonon group values should ideally be calculated as a function of the temperature [99]. However, since the phonon dispersion is here strictly 1D, the large value of Dulong-Petit limit itself guaranties a large average along-axis group velocity [89,96].

Looking at the vibrational DOS, Fig. S2 in Ref. [57], we see that the phonons fall in two classes: the lower group, bounded by the vertical dotted line at $\omega_{cut} = 381.06$ cm^{-1} and the upper group that can be interpret as optical phonons. The lower group contains phonons can be seen as connecting the acoustic phonons and vibrations at ω_{cut}. We shall refer to the latter as an effective acoustic cutoff. The average group

TABLE III. Bond length (in angstroms) between the atoms in fully relaxed ground states of single-walled armchair (ac) and zigzag (zz) Si_2BN NTs with a different chiral vector (n, m) compared with the respective bond lengths in Si_2BN 2D sheet. Small-diameter NTs are highly strained in the bond lengths in comparison to large-diameter NTs.

System	Si-Si	Si-B	Si-N	B-N
2D-sheet	2.246	1.951	1.756	1.466
AC(1,1)	2.393	2.078	1.791	1.426
AC(2,2)	2.292	2.002	1.749	1.441
AC(3,3)	2.248	1.977	1.758	1.447
AC(4,4)	2.240	1.96	1.77	1.460
AC(7,7)	2.246	1.951	1.756	1.466
ZZ(2,0)	2.325	2.037	1.789	1.451
ZZ(3,0)	2.280	2.014	1.741	1.443
ZZ(4,0)	2.261	1.996	1.746	1.438
ZZ(5,0)	2.238	1.992	1.758	1.441
ZZ(6,0)	2.239	1.958	1.760	1.457
ZZ(7,0)	2.238	1.955	1.760	1.459
ZZ(12,0)	2.244	1.951	1.756	1.466

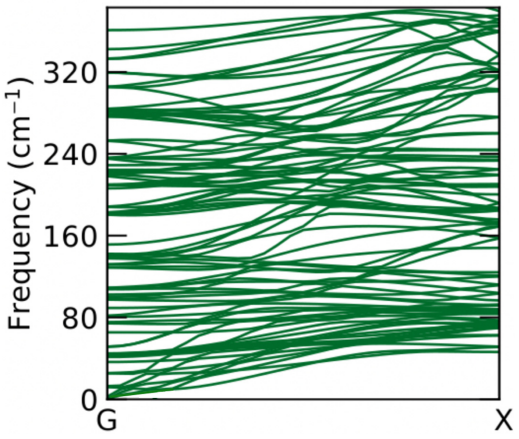

FIG. 3. Phonon dispersion profile of armchair Si_2BN (4,4) nanotube. Absence of imaginary frequencies in phonon dos show the dynamic stability of the nanotube.

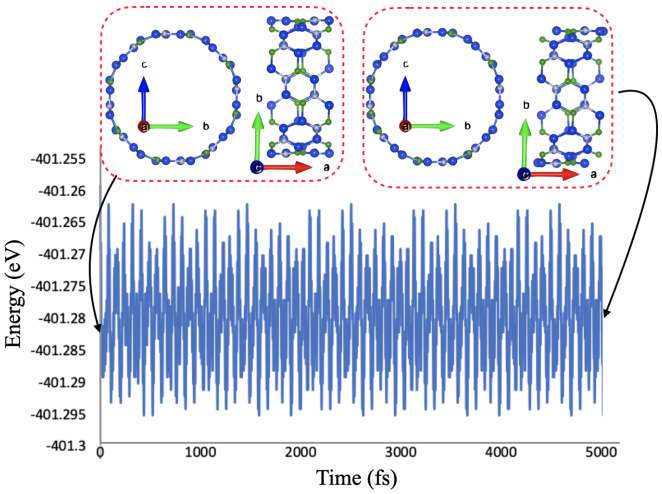

FIG. 4. Variations of the total energy for armchair (4,4) Si_2BN nanotube during first-principles molecular dynamics simulation at higher temperature 1000 K for 5 ps. The small variation in total energies documents that this nanotube is stable also at elevated temperatures. The inserts above the energy variations shows the initial and final structure during the molecular dynamics simulations with similar bond length and structure.

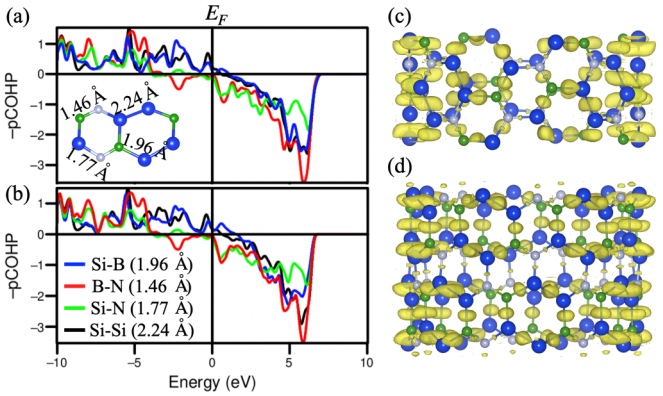

FIG. 5. Projected crystal orbital Hamilton Population (-pCOHP) analysis for (a) armchair (4,4) and (b) zigzag (7,0) Si_2BN NTs summed up over the pairs Si-Si, B-N, Si-B, and Si-N. The zero level shows the Fermi energy (E_F). The -pCOHP provides information about the contribution of a specific bond (bonding or anti bonding) to the band energy. The positive value on y axis represent the bonding contribution and negative value on y axis shows the antibonding contribution. Electron localization function of (c) armchair (4,4) and (d) zigzag (7,0) Si_2BN NT.

velocity of the transport carrying modes is clearly bounded by ω_{cut}/k, where the inverse length k=0.0775 is the propagation vector, given by the reciprocal-space distance between X and Γ.

While the ratio ω_{cut}/k is not a quantitative measure of the average group velocity, it suffices for a comparison of phonon transport in similar NT, for example carbon and Si_2BN NTs. That is, we can compare the magnitudes of ω_{cut}/k to get an indication of whether a NT is a fair heat carrier. We find that the Si_2BN value compares with the value that we also here estimate for a (11,11) C NT with similar diameter: 11.11 km/second versus 21.84 km/second.

In summary, there are good reasons to expect a significant vibrational contribution to the Si_2BN NT thermal conductivity.

Figure 4 and Fig. S3 in Ref. [57] presents an extra independent check of the NT stability that we also provide. The figure summarizes the results of an full first-principles molecular dynamics (FPMD) simulations. It shows the structure of the armchair/zigzag NT at the initial and final stages of FPMD simulation performed at 1000 K for 5 ps. The figure also shows the computed variations that we find om the total energy of the system as a function time steps. We find that this variation is minimal and that there has been no bond breaking during the MD run. The study confirms that we can also expect a degree of thermal stability, even at high temperatures.

We find, in particular, that the dynamics is characterized by the same structure that exists in the initial and final NT configurations, i.e., the bond lengths does not change. For that analysis, we extracted a few snap-shot images and then fully relaxed the ionic positions of those configuration with a regular DFT study (until the forces converged up to 0.01 eV/atom). Among those fully relaxed NT variants, we find no significant differences from the extracted structures.

Interestingly, we also learned from putting the smallest diameter NTs onto such MD-based stability test. Figure S4 of the MD shows that the armchair (2,0) NT has higher fluctuation in total energies with time in comparison to zigzag (1,1) NT. We see that as we approach the very small NTs (that have an actual dynamical instability) there are incipient fluctuations in the MD runs. In other words, the MD simulation test is able to correctly identify unstable NTs, when relevant. We consider our MD testing a robust, independent confirmation of the expected high-temperature stability for the regular-sized Si_2BN NTs.

B. Chemical bonding information

Beyond the two main-interest (normal sized) NTs, above, we have also sought a broader mapping of stability in the NTs and the size impact that will exist on properties. Since this exploration must begin with a mechanical stability analysis, we have sought a simpler tool than using a combination of both phonon calculations and FPMD simulations, for every considered Si_2BN NT.

The COHP analysis partitions the band-structure variation into contributions that identifies the binding nature, that is, nonbonding and antibonding contributions. This is done using projections on localized atomic basis sets. We use it as extracted from a projection of our planewaves DFT results, a so-called pCOHP analysis. We find that the pCOHP analysis is useful for our wider exploration and discussion. It allows us to document the extent that the NT bonding retains a pronounced covalent character even after we have imposed significant extra strain in completing the NT rolling.

Figures 5(a) and 5(b) tracks the chemical bonding as revealed in a pCOHP analysis [107,108] for the armchair (4,0) and zigzag (7,7) NTs, respectively. The inset shows the bond lengths between the atoms and color combinations for different bonding pairs. The main panels display an energy-resolved mapping of the nature of the chemical bonding that underpins

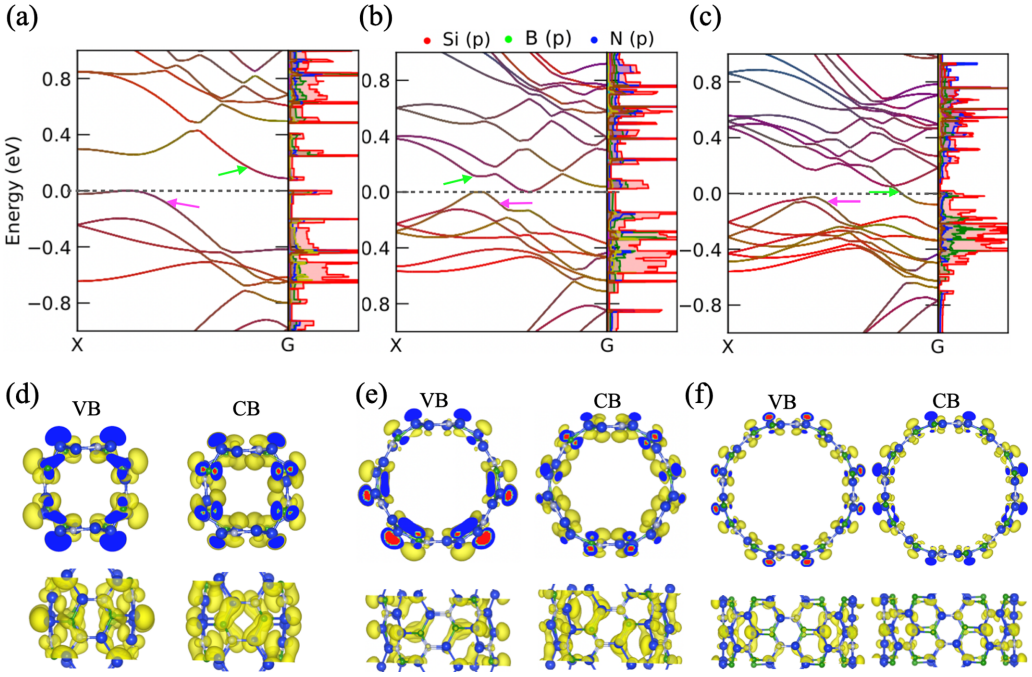

FIG. 6. (Top row) Orbital- and element-resolved comparison of the electronic band structure and corresponding projected density of states for armchair direction (a) (2,2), (b) (3,3), and (c) (4,4) NTs. We focus on the region near the Fermi level, which is set at zero noting that there is no actual Fermi level or chemical potential alignment across the structures. Pink and green arrows denote the highest valence band (VB) and lowest conduction band (CB), respectively. (Bottom row) Band-resolved mapping of the charge density below the Fermi level and probability density above the Fermi level, with (d), (e), and (f) corresponding to the system characterized in (a), (b), and (c), respectively. The orbital representation is extracted at the lowest CB (highest VB) energy location of the band-structure parts identified by green (pink) arrows. They identify the CB/VB orbital nature that defines transport properties in the set of armchair NTs that have increasing diameters.

the delocalized electronic structure [109]. Positive (negative) values reflects bonding (antibonding) contributions as the emerge on orbitals corresponding to different bonds among the constituent atoms [51].

Figures 5(a) and 5(b) shows that all the bond pairs have stable chemical bonding interactions because few anti-bonding states are located at or below the Fermi level. We can see some bonding emerging also above the Fermi level (mainly appearing from Si-Si and Si-B bonds); The presence of such bonding states implies that the conduction band is able to accumulate also some extra electrons, i.e., reflecting a metallic signature. Anti-bonding states dominates well above the Fermi level, Figs. 5(a) and 5(b), but such a character is limited to B-N bond contributions from just below the Fermi level, in both the armchair and zigzag NTs.

The corresponding integrated-COHP (ICOHP) measure has already been used to measure bond strengths in various materials [110]. The ICOHP values for Si-B, Si-Si, Si-N, and B-N bond pairs are found to be −5.74 (−5.77), −6.20 (−6.19), −6.28 (−6.25), and −8.75 (−8.69) eV for armchair (zigzag) directions, respectively. The B-N and Si-N come out to be the strongest bond-pair interaction compared to other bond pairs in the Si_2BN NT. However, it should be noted that ICOHP mainly measures the strength of the covalency of a bond, but not its ionicity.

Finally, Figs. 5(c) and 5(d) shows a map of the electron localization function (ELF), again revealing the nature of bonding between Si, B, and N atoms. The electron density is mainly localized between the Si-Si, Si-B, Si-N, and B-N atoms, which indicates that the Si-Si, Si-B, Si-N, and B-N atoms form strong covalent bonds. This observation supports the assumption of the possibility of excellent mechanical properties and the high hardness of these NTs [111,112].

C. Electronic structure and transport properties

The electronic properties of Si_2BN NTs are next discussed based on their curvature and the resulting hybridization effects [113]. We have tested for the impact of inclusion of the spin-orbit coupling and we do not find any significant difference in the electronic band structure (see Fig. S8 in Ref. [57]) for medium-size NTs. Our spin polarized calculations suggest that there is no magnetism in these NTs.

Figures 6(a)–6(c) show the projected electronic band structure and density of states for various armchair NTs. The lower panel in Figs. 6(d)–6(f) stands for the band-decomposed density probability of the first band above and below the Fermi level. This represents the density for these band dispersion between G-X.

In the upper panel of Fig. 6, armchair NTs show varying electronic properties such as semiconducting in (2,2), semimetallic in (3,3), and metallic in the larger diameter (4,4) NT. The Fermi levels or chemical potential levels are set at zero, there is no actual alignment of these levels across the structures. Table II also gives information about the chiral vector, diameter, and respective electronic properties. In the (2,2) NT, the indirect band gap was found to be 0.09 eV with a valence band (VB) maximum (VBM) in between X-G and conduction band (CB) minimum (CBM) at G point.

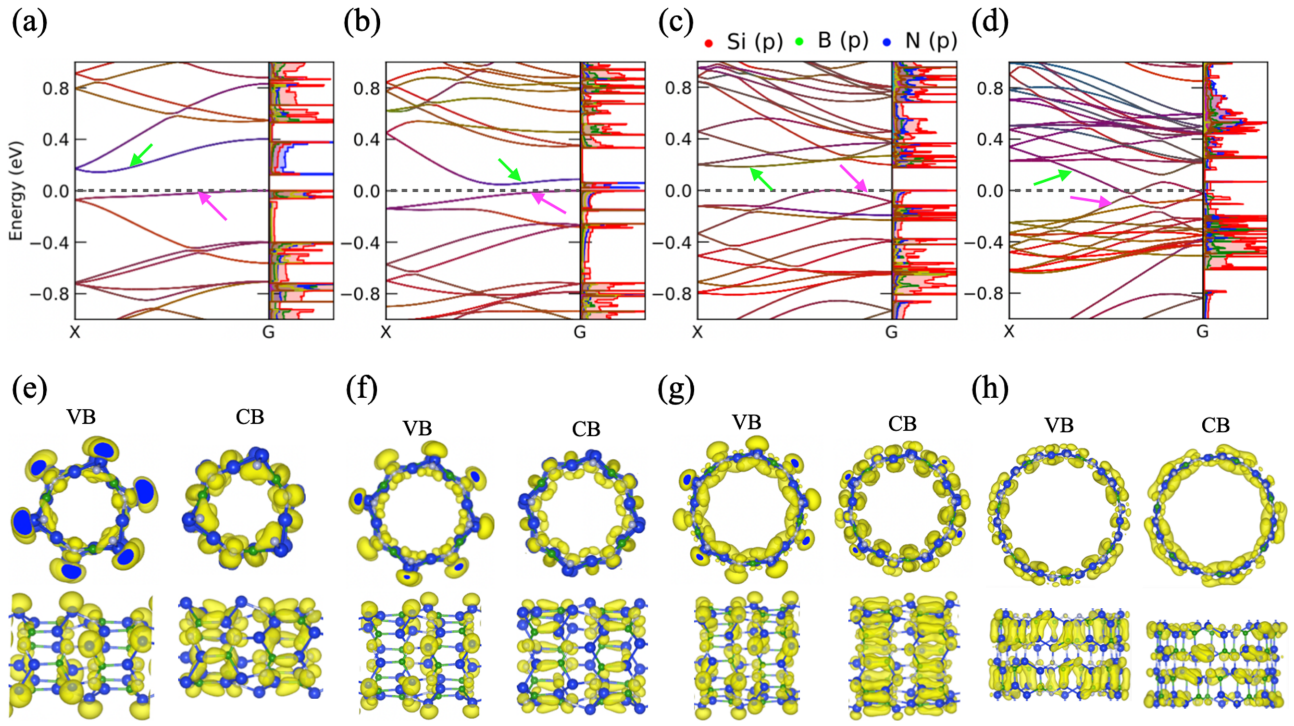

FIG. 7. Orbital- and element-resolved comparison of the electronic band structure and corresponding projected density of states for zigzag NTs (3,0), (4,0), (5,0), and (7,0), in separate columns. The set of top panels shows a traditional band-structure mapping while the set of bottom panels provides analysis of the orbital nature that defines the electrical transport; nomenclature as in corresponding analysis for the armchiar NTs, Fig. 6.

Figure 6(d) shows that the CB part that is located just above the Fermi level (shown by dotted line) arises primarily from the G point and is defined by Si-B π bonding. In contrast, the VB part that is located just below the Fermi level arises from contributions that are dominated by the π-σ hybridization in Si-B atoms, while the density at N atom is partially localized. In the case of the (3,3) NT, bands touch the Fermi level between G and X band points, reflecting a semimetallic nature of conduction. Band decomposed density in Fig. 6(e) shows that Si-Si and Si-B π bonds, which provide a downshift to the band above the Fermi. The electron/hole probability density is more localized in the Si-N bond region. In the top VB, there is still π-σ hybridization in the Si-B bond, which is confirmed by the π orbital primarily localized at the outer surface of the tube at the Si atom. A similar case was reported in the C NT [113].

For the relatively larger NT (4,4), the CB crosses the Fermi (making it metallic) and arises as dominated by Si-Si and Si-B π bonds, similar to those found in the Si_2BN planar sheet. There is a change in band dispersion because of the larger diameter of the NT. Here we find states at N atoms that are even more localized for the CB, Fig. 5(f). A similar behavior is evident in VB below the Fermi level, where a strong π bond between two silicon and one boron atoms is formed.

We also extended our transport study to the ultra-small (1,1) and large (7,7) armchair NTs (with diameters of ∼0.4 and ∼2.5 nm, respectively). It is important to note that we find very small NTs to be unstable, see Ref. [57]. Nevertheless, they are still worth investigating to fully reveal the size impact on conduction trends.

We find that these (unstable, small) armchair NTs show a metallic nature of conduction. That is a metal-type band-structure documented in Figs. S5 and S6 of Ref. [57]. It arises because of the strong curvature effect and dominant π-σ hybridization owing to structural deformations. These hybridization effects and stability are further supported by COHP in Fig. S7. A further discussion can be found in Ref. [57].

Moving to zigzag NTs, Fig. 7 shows the band structures and band decomposed density for (3,0), (4,0), (5,0), and (7,0) NTs. Electronic band gap properties along with strain energy and diameter can be seen in Table II.

The small diameter tube (3,0) shows an indirect band gap of 0.14 eV, where VBM is at G point and CBM is at X points. Figures 7(a) and 7(e) show that the highly localized π orbital on N atom dominates the CB close to Fermi level and there is π-σ hybridization Si-B. There is also a π bond formation at an inner surface of the tube in between the second nearest Si-B atoms. The quasi flat VB component just below the Fermi level is dominated by localized states at alternate Si atoms, which has localization at the outer surface of the tube. The VB is partially constituted by the π-π interaction in alternate Si and B atoms at the inner surface of the tube and localized states at N atoms. This dispersionless feature comes from a highly distorted structure, where buckling is such that one Si atom in a hexagonal unit comes out of the plane resulting in the strongly localized states. We find that the strong localization is responsible for the band gap opening.

Increasing the diameter, we next consider the (4,0) NT. Here, the lowest CB component is pushed down towards the Fermi level resulting in a reduced indirect band gap of 0.05 eV.

The VBM and CBM are at the G point and in between the G and X points, respectively, in Fig. 7(b). It is clear from Fig. 7(f) that the lowest CB is still dominated by the π orbital localized in N atoms and Si-B π bonds. Unlike (3,0) tube, this lacks the inner surface Si-B bonds between second nearest neighbors due to large diameter and shows less buckling effect. The quasiflat band in VB has a localized behavior out side Si and N atoms similar to (3,0) NT in Fig. 7(e).

For the (5,0) NT, Fig. 7(c), we find that the CBM is located at X point and the VBM is located in between the G-X with an indirect band gap of 0.18 eV. Figure 7(g) shows a strong π bond behavior in Si-B bond at both the inner and outer surface of the tube and localized state at the out of surface Si atom in the lowest CB. However, there is less buckling in comparison to (3,0) and (4,0) NTs. There is a minimal contribution from the N atom as can also be seen in Fig. 7(c). The VB close to the Fermi level mainly arises by the localized state on the Si atom at the outer surface and Si-Si π bonds in the inner surface of the tube. There are also contributions from B-N π bonds.

Figure 7(d) shows that the CBM and VBM come close to each and form conelike behavior in the ∼1.5 nm diameter NT (7,0). A Band decomposed mapping of density in Fig. 7(g) shows that Si-Si and B-N π bond nature is restored in the conduction band. The VB arise from Si-B π bonds, which is similar to those of the Si_2BN sheet. The highly delocalized π bond behavior is responsible for a metallic nature in the (7,0) NT. A similar electronic structure was also found in (6,0) and even larger diameter tubes (12,0). The smallest possible diameter zigzag NT (2,0) also shows similar semiconducting behavior due to the strongly localized state around the Fermi level as described in Ref. [57].

The effect of even larger diameters is also investigated for the ∼2.5 nm diameter armchair and zigzag NTs. Similar to the Si_2BN sheet, these NTs remain metallic with more states around the Fermi level and can be seen in Figs. S9 and S10. We find band-projected densities and a bonding nature that are similar to those found in a planar Si_2BN sheet.

Interestingly, the small-diameter NTs are found to be semiconducting. This behavior is different than what is found in carbon NTs, BC_2N, and Silicene NTs [113–115]. The hybridization is the key to understanding the metallic behavior in carbon NTs at small diameters [113]. We find a different Si_2BN behavior (in the small-diameter limit) because the constituent elements have varying electronegativity values.

At a small diameter, the Si_2BN hexagonal ring gets further distorted and buckles out of the plane with stretched bonds. This gives density localization despite the strong possibility of the hybridization due to curvature. Similar behavior was reported by Shukla *et al.* [51], where puckered Si_2BN sheet showed semiconducting behavior. In the large-diameter tubes, bond angles further deviate from the ideal 120° on the NT wall, this results in an increase of the π-σ orbital interaction in comparison to the planer sheet and alter the reactivity of the NT walls with bonding strengths varying with the binding sites. Our Bader charge analysis for armchair (4,0) nanotube suggests that the Si sites are expected to be more reactive (sticky) compared to other sites. As such, the new NTs have a different behavior than the distinct chemistry of C NTs and hBN NTs.

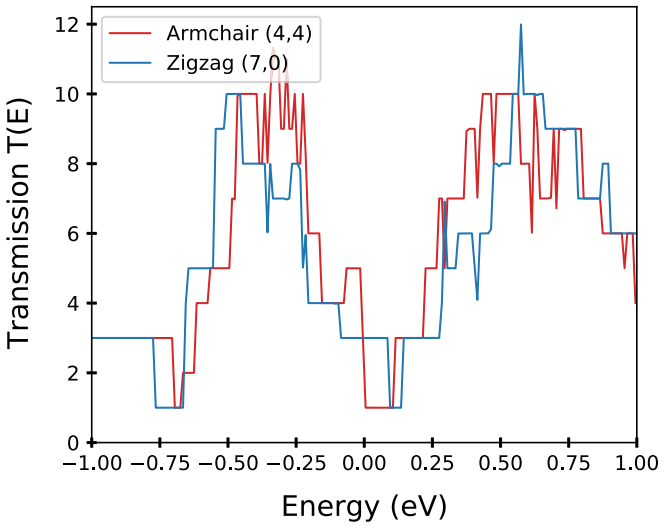

FIG. 8. Electron transport behavior at zero-bias transmission in the armchair Si_2BN NT (4,4) (green color) and the zigzag (7,0) NT (red color). We find a stepwise transmission that can be correlated with the associated bands in electronic band structure these NTs, see text. Both NT have essentially the same diameter ∼1.5 nm.

To further evaluate the electrical conductivity we also provide a set of nonequilibrium Green function (NEGF) transport calculations [116–130]. There exist a rigorous Lippmann-Schwinger (LS) scattering formalism [116,119,129,130] for such studies. Even if we use exchange-correlation functionals crafted for ground-state DFT [131], our computation of effective single-particle LS orbitals have a well-defined physics meaning in terms of Friedel scattering phase shifts and grand-canonical ensemble DFT [130,132–134]. In the ballistic transport case, electron-phonon and phonon-phonon scattering is ignored and computation of the electron transmission $T(E)$ essentially reduces to a counting of the number of available conduction channels, each having some probability for being affected by elastic scattering. Each channel carries a so-called conduction quanta, $G_0 = 2e^2/h$, where e is electron charge and h is plank's constant. The resulting electron conduction can thus be asserted from $G = G_0 T(E)$. This simple ballistic-transport characterization [125,126,131,135] can be used for a first assessment of the Si_2BN NT electron-transport performance.

Figure 8 reports our electron transport study of the armchair (4,4) and zigzag (7,0) NTs, both having an ∼1.5 nm diameter. We find that the computed transmission function $T(E)$ has essentially regular steps, reflecting that elastic scattering does not strongly impede the electrons dynamics across central Si_2BN model region in our NEGF calculation setup, See Fig. S11 in Ref. [57].

Figure 8 shows that the transmission is lower at the Fermi level for the armchair case than for the zigzag case. This is also expected from from the band structure results shown in Figs. 6 and 7. The zigzag (armchair) NT has three (one) transmission channel at the Fermi level. However, we find that applying a bias can significantly increase the armchair NT transmission. In contrast, the zigzag NT behavior is a flat transmission line

above the Fermi level 0 to 0.1 eV. This is due to a cone-type band dispersion around the Fermi level.

Finally, we consider the electronic part of thermal conductivity. In metallic systems the contribution is directly proportional to the electrical conductivity, assuming that the Wiedemann-Franz law [136] remains valid also for our low-dimensional focus. We therefore expects that also the electronic part of thermal conductivity will be high in Si_2BN nanotubes [137].

IV. CONCLUSIONS

Successful synthesis of theoretically predicted materials motivates continued and intensified use of high level of theoretical methods for further explorations of new materials. Herein, with DFT-based first-principles method, we systematically investigated the structural stability, and electronic properties of armchair and zigzag Si_2BN NT geometries. We also presented analysis of the chemical-bonding nature between the elements. Our calculations reveal that Si_2BN NT conformations can yield advantages resembling those that have previously been reported for Carbon and BC_2N NTs. Specially, the NT geometry gives us the option to control and adjust the structural and electronic properties relative to those that characterize the pristine sheets.

We predict that Si_2BN NTs are highly stable as reflected in cohesive energies in comparison to the silicon, phosphorene and boron based NTs. The stability prediction is confirmed by our calculations of strain energies, phonon dispersion spectra, and first-principles molecular dynamics (FPMD) at 1000 K. Our COHP analysis suggests a strong covalent bonding between the Si-Si, Si-B/N, and B-N atoms, persist across the range of NT sizes. These findings make it plausible that one can synthesize Si_2BN also in NT conformations: The bonds can withstand large additional strain.

The presence of distorted hexagonal patterns and covalent radii differences makes the properties of Si_2BN in NT conformations even richer. Si_2BN NTs show a semiconducting behavior at small radius and a metallic behavior at large radius unlike the carbon NTs. This is true despite the possibility of strong hybridization in small-radius NTs. We have explained this prediction in terms of differences in varying electronegativities of Si, B, and N elements.

Our quantum transport investigation reveals that the armchair NT shows higher conductivity than the zigzag NT at low bias regime. From the phonon, electronic structure and transport studies, we conclude that electronic part of the thermal conductivity will be high in Si_2BN NTs. Taken together these findings suggest that rolling NT geometries may work for electronics but not for thermoelectric applications.

Overall we conclude that the rolling of Si_2BN sheets into NT conformations provides options for further engineering of properties. It is our hope that our study can thus contribute to the motivation for Si_2BN synthesis and may find potential applications in nanoscale devices, batteries, sensing, hydrogen storage, and photocatalysis.

ACKNOWLEDGMENTS

D.S., N.K., and R.A. acknowledge Swedish Research Council (VR-2016-06014 and VR-2020-04410) and J. Gust. Richert stiftelse, Sweden (2021-00665) for financial support. V.S. and P.H. acknowledge the Swedish Foundation for Strategic Research (SSF) through Grant No. IMF17-0324, as well as the Chalmers Area-of-Advance-Materials theory & -Production theory activities as well as Sweden's innovation agency Vinnova through Project No. 2020-05179. The authors gratefully acknowledge computational resources from the Swedish National Infrastructure for Computing SNIC (2021/1-42 as well as SNIC2020-3-13, SNIC2021-3-18), HPC2N, and C3SE.

[1] Y. Cheng, B. Ren, K. Xu, I. Jeerapan, H. Chen, Z. Li, and J. Z. Ou, Recent progress in intrinsic and stimulated room-temperature gas sensors enabled by low-dimensional materials, J. Mater. Chem. C **9**, 3026 (2021).

[2] D. Singh, V. Shukla, N. Khossossi, A. Ainane, and R. Ahuja, Harnessing the unique properties of mxenes for advanced rechargeable batteries, J. Phys. Energy **3**, 012005 (2021).

[3] V. Shukla, R. L. Kumawat, N. K. Jena, B. Pathak, and R. Ahuja, Electronic and transport properties of bilayer phosphorene nanojunction: Effect of paired substitution doping, ACS Appl. Electron. Mater. **3**, 733 (2021).

[4] V. Shukla, Computational studies of 2D materials : Application to energy storage and electron transport in nanoscale devices, Ph.D. thesis, Uppsala University, 2019

[5] F. Xia, H. Wang, D. Xiao, M. Dubey, and A. Ramasubramaniam, Two-dimensional material nanophotonics, Nat. Photonics **8**, 899 (2014).

[6] D. Singh, V. Shukla, and R. Ahuja, Optical excitations and thermoelectric properties of two-dimensional holey graphene, Phys. Rev. B **102**, 075444 (2020).

[7] S. Umrao, A. Maurya, V. Shukla, A. Grigoriev, R. Ahuja, M. Vinayak, R. Srivastava, P. Saxena, I.-K. Oh, and A. Srivastava, Anticarcinogenic activity of blue fluorescent hexagonal boron nitride quantum dots: as an effective enhancer for dna cleavage activity of anticancer drug doxorubicin, Mater. Today Bio. **1**, 100001 (2019).

[8] D. Singh, V. Shukla, P. K. Panda, Y. K. Mishra, H.-G. Rubahn, and R. Ahuja, Carbon-phosphide monolayer with high carrier mobility and perceptible i–v response for superior gas sensing, New J. Chem. **44**, 3777 (2020).

[9] A. Jain, Y. Shin, and K. A. Persson, Computational predictions of energy materials using density functional theory, Nat. Rev. Mater. **1**, 15004 (2016).

[10] N. Marzari, A. Ferretti, and C. Wolverton, Electronic-structure methods for materials design, Nat. Mater. **20**, 736 (2021).

[11] J. W. Mintmire and C. T. White, Universal Density of States for Carbon Nanotubes, Phys. Rev. Lett. **81**, 2506 (1998).

[12] L. Cheng, J. Meng, X. Pan, Y. Lu, X. Zhang, M. Gao, Z. Yin, D. Wang, Y. Wang, J. You *et al.*, Two-dimensional hexagonal boron–carbon–nitrogen atomic layers, Nanoscale **11**, 10454 (2019).

[13] F. Qitang, Y. Linghao, W. T. Matthias, O. Krejčí, D. Stavrina, S. R. Kachel, C. Mengyi, A. S. Foster, K. Ulrich, L. Peter, and

J. M. Gottfried, Biphenylene network: A nonbenzenoid carbon allotrope, Science **372**, 852 (2021).

[14] H. Li, R. Y. Tay, S. H. Tsang, L. Jing, M. Zhu, F. N. Leong, and E. H. T. Teo, Composition-controlled synthesis and tunable optical properties of ternary boron carbonitride nanotubes, RSC Adv. **7**, 12511 (2017).

[15] Y. Wang, J. Zhang, X. Wang, M. Antonietti, and H. Li, Boron- and fluorine-containing mesoporous carbon nitride polymers: Metal-free catalysts for cyclohexane oxidation, Angew. Chem., Int. Ed. **49**, 3356 (2010).

[16] K. Raidongia, A. Nag, K. Hembram, U. Waghmare, R. Datta, and C. Rao, BCN: A graphene analogue with remarkable adsorptive properties, Chem. A: Eur. J. **16**, 149 (2010).

[17] T. Taguchi, N. Igawa, H. Yamamoto, and S. Jitsukawa, Synthesis of silicon carbide nanotubes, J. Am. Ceram. Soc. **88**, 459 (2005).

[18] K. W. Völger, E. Kroke, C. Gervais, T. Saito, F. Babonneau, R. Riedel, Y. Iwamoto, and T. Hirayama, B/C/N materials and B_4C synthesized by a non-oxide sol-gel process, Chem. Mater. **15**, 755 (2003).

[19] R. Bian, C. Li, Q. Liu, G. Cao, Q. Fu, P. Meng, J. Zhou, F. Liu, and Z. Liu, Recent progress in the synthesis of novel two-dimensional van der Waals materials, Natl. Sci. Rev. **9**, 1 (2021).

[20] X. Zhang, T. Wu, H. Wang, R. Zhao, H. Chen, T. Wang, P. Wei, Y. Luo, Y. Zhang, and X. Sun, Boron nanosheet: an elemental two-dimensional (2D) material for ambient electrocatalytic N_2-to-NH_3 fixation in neutral media, ACS Catal. **9**, 4609 (2019).

[21] A. Molle, C. Grazianetti, L. Tao, D. Taneja, M. H. Alam, and D. Akinwande, Silicene, silicene derivatives, and their device applications, Chem. Soc. Rev. **47**, 6370 (2018).

[22] A. E. G. Mikkelsen, F. T. Bölle, K. S. Thygesen, T. Vegge, and I. E. Castelli, Band structure of moste janus nanotubes, Phys. Rev. Mater. **5**, 014002 (2021).

[23] S. Enouz, O. Stéphan, J.-L. Cochon, C. Colliex, and A. Loiseau, C-BN patterned single-walled nanotubes synthesized by laser vaporization, Nano Lett. **7**, 1856 (2007).

[24] B. Ni, H. Liu, P.-P. Wang, J. He, and X. Wang, General synthesis of inorganic single-walled nanotubes, Nat. Commun. **6**, 8756 (2015).

[25] J. H. Lehman, K. E. Hurst, G. Singh, E. Mansfield, J. D. Perkins, and C. L. Cromer, Core–shell composite of sicn and multiwalled carbon nanotubes from toluene dispersion, J. Mater. Sci. **45**, 4251 (2010).

[26] J. Qiao, F. Song, J. Hu, D. Huo, J. Yuan, J. Shen, L. Niu, and A. jun Wang, Ultrathin mosse alloy nanosheets anchored on carbon nanotubes as advanced catalysts for hydrogen evolution, Inte. J. Hydrogen Energy **44**, 16110 (2019).

[27] Y. Ben-Shimon, V. Bhingardive, E. Joselevich, and A. Ya'akobovitz, Self-sensing WS_2 nanotube torsional resonators, Nano Lett. **22**, 8025 (2022).

[28] M. Li, X. Peng, X. Liu, H. Wang, S. Zhang, and G. Hu, Single-atom niobium doped bcn nanotubes for highly sensitive electrochemical detection of nitrobenzene, RSC Adv. **11**, 28988 (2021).

[29] Y. Fang and X. Wang, Metal-free boron-containing heterogeneous catalysts, Angew. Chem., Int. Ed. **56**, 15506 (2017).

[30] S. Wang, E. Iyyamperumal, A. Roy, Y. Xue, D. Yu, and L. Dai, Vertically aligned BCN nanotubes as efficient metal-free electrocatalysts for the oxygen reduction reaction: A synergetic effect by co-doping with boron and nitrogen, Angew. Chem., Int. Ed. **50**, 11756 (2011).

[31] Z. Zhang, C. Shao, Y. Sun, J. Mu, M. Zhang, P. Zhang, Z. Guo, P. Liang, C. Wang, and Y. Liu, Tubular nanocomposite catalysts based on size-controlled and highly dispersed silver nanoparticles assembled on electrospun silica nanotubes for catalytic reduction of 4-nitrophenol, J. Mater. Chem. **22**, 1387 (2012).

[32] Y. P. Zhu, T. Y. Ma, M. Jaroniec, and S. Z. Qiao, Self-templating synthesis of hollow Co_3O_4 microtube arrays for highly efficient water electrolysis, Angew. Chem., Int. Ed. **56**, 1324 (2017).

[33] H. Wang, S. Zhuo, Y. Liang, X. Han, and B. Zhang, General self-template synthesis of transition-metal oxide and chalcogenide mesoporous nanotubes with enhanced electrochemical performances, Angew. Chem. **128**, 9201 (2016).

[34] E. Iyyamperumal, S. Wang, and L. Dai, Vertically aligned bcn nanotubes with high capacitance, ACS Nano **6**, 5259 (2012).

[35] K. Zhang, Y. Guo, Q. Ji, A.-Y. Lu, C. Su, H. Wang, A. A. Puretzky, D. B. Geohegan, X. Qian, S. Fang *et al.*, Enhancement of van der waals interlayer coupling through polar janus mosse, J. Am. Chem. Soc. **142**, 17499 (2020).

[36] K. Zhang, Y. Guo, D. T. Larson, Z. Zhu, S. Fang, E. Kaxiras, J. Kong, and S. Huang, Spectroscopic signatures of interlayer coupling in janus $MoSSe/MoS_2$ heterostructures, ACS Nano **15**, 14394 (2021).

[37] A. Taufik, Y. Asakura, T. Hasegawa, and S. Yin, $MoS_2 - xSe_x$ nanoparticles for no detection at room temperature, ACS Appl. Nano Mater. **4**, 6861 (2021).

[38] Z. Tian, N. Chui, R. Lian, Q. Yang, W. Wang, C. Yang, D. Rao, J. Huang, Y. Zhang, F. Lai *et al.*, Dual anionic vacancies on carbon nanofiber threaded mosse arrays: a free-standing anode for high-performance potassium-ion storage, Energy Storage Mater. **27**, 591 (2020).

[39] J. Gao, Y. Li, Y. Liu, S. Jiao, J. Li, G. Wang, S. Zeng, and G. Zhang, The dual-function sacrificing template directed formation of MoS_2/C hybrid nanotubes enabling highly stable and ultrafast sodium storage, J. Mater. Chem. A **7**, 18828 (2019).

[40] V. Shukla, J. Warna, N. K. Jena, A. Grigoriev, and R. Ahuja, Toward the realization of 2D borophene based gas sensor, J. Phys. Chem. C **121**, 26869 (2017).

[41] Z.-Q. Wang, T.-Y. Lü, H.-Q. Wang, Y. P. Feng, and J.-C. Zheng, Review of borophene and its potential applications, Front. Phys. **14**, 33403 (2019).

[42] V. Shukla, R. B. Araujo, N. K. Jena, and R. Ahuja, Borophene's tryst with stability: exploring 2D hydrogen boride as an electrode for rechargeable batteries, Phys. Chem. Chem. Phys. **20**, 22008 (2018).

[43] V. Shukla, A. Grigoriev, and R. Ahuja, Rectifying behavior in twisted bilayer black phosphorus nanojunctions mediated through intrinsic anisotropy, Nanoscale Advances **2**, 1493 (2020).

[44] A. N. Andriotis, E. Richter, and M. Menon, Prediction of a new graphenelike Si_2BN solid, Phys. Rev. B **93**, 081413(R) (2016).

[45] E. D. Sandoval, S. Hajinazar, and A. N. Kolmogorov, Stability of two-dimensional BN-Si structures, Phys. Rev. B **94**, 094105 (2016).

[46] Z. G. Fthenakis, M. Jaishi, B. Narayanan, A. N. Andriotis, and M. Menon, High temperature stability, metallic character and bonding of the Si_2BN planar structure, J. Phys.: Condens. Matter **33**, 165001 (2021).

[47] S. Angizi, M. A. Akbar, M. Darestani-Farahani, and P. Kruse, Review—two-dimensional boron carbon nitride: A comprehensive review, ECS J. Solid State Sci. Technol. **9**, 083004 (2020).

[48] J. O. Sofo, A. S. Chaudhari, and G. D. Barber, Graphane: A two-dimensional hydrocarbon, Phys. Rev. B **75**, 153401 (2007).

[49] D. Singh, S. K. Gupta, Y. Sonvane, and R. Ahuja, High performance material for hydrogen storage: Graphenelike Si_2BN solid, Inte. J. Hydrogen Energy **42**, 22942 (2017).

[50] S. Hu, Y. Yong, C. Li, Z. Zhao, H. Jia, and Y. Kuang, Si_2BN monolayers as promising candidates for hydrogen storage, Phys. Chem. Chem. Phys. **22**, 13563 (2020).

[51] V. Shukla, R. B. Araujo, N. K. Jena, and R. Ahuja, The curious case of two dimensional Si_2BN: a high-capacity battery anode material, Nano Energy **41**, 251 (2017).

[52] T. Hussain, D. Singh, S. K. Gupta, A. Karton, Y. Sonvane, and R. Ahuja, Efficient and selective sensing of nitrogen-containing gases by Si_2BN nanosheets under pristine and pre-oxidized conditions, Appl. Surf. Sci. **469**, 775 (2019).

[53] D. Singh, S. Chakraborty, and R. Ahuja, Emergence of Si_2BN monolayer as efficient her catalyst under co-functionalization influence, ACS Appl. Energy Mater. **2**, 8441 (2019).

[54] D. Singh, S. K. Gupta, Y. Sonvane, T. Hussain, and R. Ahuja, Achieving ultrahigh carrier mobilities and opening the band gap in two-dimensional Si_2BN, Phys. Chem. Chem. Phys. **20**, 21716 (2018).

[55] Z. G. Fthenakis and M. Menon, Structural deformations and mechanical properties of Si_2BN under uniaxial and uniform biaxial strain in comparison with graphene: An *ab initio* study, Phys. Rev. B **99**, 205302 (2019).

[56] H. Mahida, D. Singh, Y. Sonvane, P. Thakor, R. Ahuja, and S. K. Gupta, The influence of edge structure on the optoelectronic properties of Si_2BN quantum dot, J. Appl. Phys. **126**, 233104 (2019).

[57] See Supplemental Material at http://link.aps.org/supplemental/10.1103/PhysRevMaterials.6.116001 for the details of phonon density of states, molecular dynamics at small diameter NTs, electronic structure of layered Si_2BN, electronic structure and COHP analysis of small diameter NTs, and schematic representation for the set up of quantum transport calculation.

[58] M. Dion, H. Rydberg, E. Schröder, D. C. Langreth, and B. I. Lundqvist, Van der Waals Density Functional for General Geometries, Phys. Rev. Lett. **92**, 246401 (2004).

[59] K. Berland and P. Hyldgaard, Analysis of van der Waals density functional components: Binding and corrugation of benzene and C_{60} on boron nitride and graphene, Phys. Rev. B **87**, 205421 (2013).

[60] K. Berland, C. A. Arter, V. R. Cooper, K. Lee, B. I. Lundqvist, E. Schröder, T. Thonhauser, and P. Hyldgaard, van der Waals density functionals built upon the electron-gas tradition: Facing the challenge of competing interactions, J. Chem. Phys. **140**, 18A539 (2014).

[61] K. Berland, V. R. Cooper, K. Lee, E. Schröder, T. Thonhauser, P. Hyldgaard, and B. I. Lundqvist, van der Waals forces in density functional theory: A review of the vdW-DF method, Rep. Prog. Phys. **78**, 066501 (2015).

[62] T. Thonhauser, S. Zuluaga, C. A. Arter, K. Berland, E. Schröder, and P. Hyldgaard, Spin Signature of Nonlocal Correlation Binding in Metal-Organic Frameworks, Phys. Rev. Lett. **115**, 136402 (2015).

[63] A. N. Mehta, W. Mu, M. Murugesan, Y. Jiao, Y. Fu, P. Hyldgaard, and J. Liu, Understanding noninvasive charge transfer doping of graphene: A comparative study, J. Mater. Sci: Mat. Elec. **29**, 5239 (2018).

[64] P. Hyldgaard, Y. Jiao, and V. Shukla, Screening nature of the van der waals density functional method: A review and analysis of the many-body physics foundation, J. Phys.: Condens. Matter **32**, 393001 (2020).

[65] P. Hohenberg and W. Kohn, Inhomogeneous electron gas, Phys. Rev. **136**, B864 (1964).

[66] G. Kresse and J. Furthmüller, Efficient iterative schemes for ab initio total-energy calculations using a plane-wave basis set, Phys. Rev. B **54**, 11169 (1996).

[67] J. P. Perdew, K. Burke, and Y. Wang, Generalized gradient approximation for the exchange-correlation hole of a many-electron system, Phys. Rev. B **54**, 16533 (1996).

[68] C. M. Frostenson, E. J. Granhed, V. Shukla, P. A. Olsson, E. Schröder, and P. Hyldgaard, Hard and soft materials: Putting consistent van der waals density functionals to work, Electron. Struct. **4**, 014001 (2022).

[69] G. Henkelman, A. Arnaldsson, and H. Jónsson, A fast and robust algorithm for bader decomposition of charge density, Comput. Mater. Sci. **36**, 354 (2006).

[70] G. J. Martyna, M. L. Klein, and M. Tuckerman, Nosé–hoover chains: The canonical ensemble via continuous dynamics, J. Chem. Phys. **97**, 2635 (1992).

[71] K. Mathew, R. Sundararaman, K. Letchworth-Weaver, T. Arias, and R. G. Hennig, Implicit solvation model for density-functional study of nanocrystal surfaces and reaction pathways, J. Chem. Phys. **140**, 084106 (2014).

[72] S. Maintz, V. L. Deringer, A. L. Tchougréeff, and R. Dronskowski, Lobster: A tool to extract chemical bonding from plane-wave based dft (2016).

[73] N. Papior, N. Lorente, T. Frederiksen, A. García, and M. Brandbyge, Improvements on non-equilibrium and transport green function techniques: The next-generation transiesta, Comput. Phys. Commun. **212**, 8 (2017).

[74] J. M. Soler, E. Artacho, J. D. Gale, A. García, J. Junquera, P. Ordejón, and D. Sánchez-Portal, The siesta method for ab initio order-n materials simulation, J. Phys.: Condens. Matter **14**, 2745 (2002).

[75] N. Troullier and J. L. Martins, Efficient pseudopotentials for plane-wave calculations, Phys. Rev. B **43**, 1993 (1991).

[76] Y. Miyamoto, A. Rubio, M. L. Cohen, and S. G. Louie, Chiral tubules of hexagonal Bc_2N, Phys. Rev. B **50**, 4976 (1994).

[77] M. Fazilaty, M. Pourahmadi, M. R. Shayesteh, and S. Hashemian, Investigating and comparing structural, electronic and optical properties of χ3-borophene in monolayer, nanoribbon and nanotube modes as a transparent metal, J. Phys. Chem. Solids **148**, 109683 (2021).

[78] C.-H. Zhang and B. Chen, The chirality of metal-encapsulated silicene-like nanotubes, Fullerenes, Nanotubes Carbon Nanostructures **25**, 699 (2017).

[79] R. Bhuvaneswari, V. Nagarajan, and R. Chandiramouli, Molecular interaction of oxytetracycline and sulfapyridine on blue phosphorene nanotubes: A first-principles insight, Phys. Lett. A **394**, 127198 (2021).

[80] H. Shin, S. Kang, J. Koo, H. Lee, J. Kim, and Y. Kwon, Cohesion energetics of carbon allotropes: Quantum monte carlo study, J. Chem. Phys. **140**, 114702 (2014).

[81] L. A. Girifalco, M. Hodak, and R. S. Lee, Carbon nanotubes, buckyballs, ropes, and a universal graphitic potential, Phys. Rev. B **62**, 13104 (2000).

[82] A. R. Juárez, E. C. Anota, H. H. Cocoletzi, J. S. Ramírez, and M. Castro, Stability and electronic properties of armchair boron nitride/carbon nanotubes, Fullerenes, Nanotubes and Carbon Nanostructures **25**, 716 (2017).

[83] B. Kang and J. Y. Lee, Electronic properties of α-graphyne nanotubes, Carbon **84**, 246 (2015).

[84] Y. Xiao, Specific heat of single-walled carbon nanotubes: A lattice dynamics study, J. Phys. Soc. Jpn. **72**, 2256 (2003).

[85] H. Einollahzadeh, S. M. Fazeli, and R. S. Dariani, Studying the electronic and phononic structure of penta-graphane, Sci. Tech. Adv. Mater. **17**, 610 (2016).

[86] G. K. Madsen and D. J. Singh, Boltztrap. a code for calculating band-structure dependent quantities, Comput. Phys. Commun. **175**, 67 (2006).

[87] Y. V. Gusev, The quasi-low temperature behaviour of specific heat, R. Soc. Open Sci. **6**, 171285 (2019).

[88] M. M. Petit and Dulong, Research on some important points of heat theory, The Philosophical Magazine **54**, 267 (1819).

[89] P. Hyldgaard and G. D. Mahan, Phonon Knudsen flow in AlAs/GaAs superlattice, in *Thermal Conductivity 23*, edited by K. E. Wilkes, R. B. Dinwiddie, and R. S. Graves (Technomic Publishing Company, CRT Press, Lancaster, PA, 1996).

[90] G. Chen, Nonlocal and nonequilibrium heat conduction in the vicinity of nanopparticles, J. Heat Trans. **118**, 539 (1996).

[91] P. Hyldgaard and G. D. Mahan, Phonon superlattice transport, Phys. Rev. B **56**, 10754 (1997).

[92] G. Chen, Size and interface effects on thermal conductivity of superlattices and periodic thin-film structures, J. Heat Trans. **119**, 220 (1997).

[93] A. Balandin and K. L. Wang, Significant descrease of the lattice thermal conductivity due to phonon confinement in a free-standing semiconductor quantum well, Phys. Rev. B **58**, 1544 (1998).

[94] G. Chen, Thermal conductivity and ballistic phonon transport in the cross-plane direction of superlattices, Phys. Rev. B **57**, 14958 (1998).

[95] E. Ziambaras and P. Hyldgaard, Thermal transport in SiC nanostructures, Mater. Sci. Eng. C **25**, 635 (2005).

[96] E. Ziambaras and P. Hyldgaard, Phonon Knudsen flow in nanostructured semiconductor systems, J. Appl. Phys. **99**, 054303 (2006).

[97] D. G. Cahill, W. K. Ford, K. E. Goodson, G. D. Mahan, A. Majumbar, H. J. Maris, R. Merlin, and S. Phillpot, Nanoscale thermal transport, J. Appl. Phys. **93**, 793 (2003).

[98] D. Singh and R. Ahuja, Dimensionality effects in high-performance thermoelectric materials: Computational and experimental progress in energy harvesting applications, WIREs: Computational Molecular Science **12**, e1547 (2022).

[99] P. Erhart, P. Hyldgard, and D. Linroth, Microscopic origin of thermal conductivity reduction in disordered van der Waals solids., Chem. Mater. **27**, 5511 (2015).

[100] J. X. Cao, X. H. Yan, Y. Xiao, Y. Tang, and J. W. Ding, Exact study of lattice dynamics of single-walled carbon nanotubes, Phys. Rev. B **67**, 045413 (2003).

[101] S. Zhang, M. Xia, S. Zhao, T. Xu, and E. Zhang, Specific heat of single-walled carbon nanotubes, Phys. Rev. B **68**, 075415 (2003).

[102] S. Lee, K. Esfarjani, T. Luo, J. Zhou, Z. Tian, and G. Chen, Resonant bonding leads to low lattice thermal conductivity, Nat. Commun. **5**, 3525 (2014).

[103] E. J. Granhed, G. Wahnström, and P. Hyldgaard, $BaZrO_3$ stability under pressure: The role of nonlocal exchange and correlation, Phys. Rev. B **101**, 224105 (2020).

[104] M. Sajjad, N. Singh, S. Sattar, S. De Wolf, and U. Schwingenschlögl, Ultralow lattice thermal conductivity and thermoelectric properties of monolayer Tl_2O, ACS Appl. Energy Mater. **2**, 3004 (2019).

[105] X. Gu and R. Yang, Phonon transport in single-layer transition metal dichalcogenides: A first-principles study, Appl. Phys. Lett. **105**, 131903 (2014).

[106] M. Sajjad and N. Singh, The impact of electron–phonon coupling on the figure of merit of Nb_2SiTe_4 and Nb_2GeTe_4 ternary monolayers, Phys. Chem. Chem. Phys. **23**, 15613 (2021).

[107] R. Dronskowski and P. E. Bloechl, Crystal orbital hamilton populations (COHP): energy-resolved visualization of chemical bonding in solids based on density-functional calculations, J. Phys. Chem. **97**, 8617 (1993).

[108] H. A. Eivari, S. A. Ghasemi, H. Tahmasbi, S. Rostami, S. Faraji, R. Rasoulkhani, S. Goedecker, and M. Amsler, Two-dimensional hexagonal sheet of TIO_2, Chem. Mater. **29**, 8594 (2017).

[109] V. L. Deringer, W. Zhang, P. Rausch, R. Mazzarello, R. Dronskowski, and M. Wuttig, A chemical link between Ge–Sb–Te and In–Sb–Te phase-change materials, J. Mater. Chem. C **3**, 9519 (2015).

[110] M. Khazaei, J. Wang, M. Estili, A. Ranjbar, S. Suehara, M. Arai, K. Esfarjani, and S. Yunoki, Novel mab phases and insights into their exfoliation into 2D mbenes, Nanoscale **11**, 11305 (2019).

[111] T. Liao, J. Wang, and Y. Zhou, Chemical bonding and mechanical properties of M_2AC (M= Ti, V, Cr, A= Al, Si, P, S) ceramics from first-principles investigations, J. Mater. Res. **24**, 556 (2009).

[112] M. Naebe, J. Wang, A. Amini, H. Khayyam, N. Hameed, L. H. Li, Y. Chen, and B. Fox, Mechanical property and structure of covalent functionalised graphene/epoxy nanocomposites, Sci. Rep. **4**, 4375 (2014).

[113] X. Blase, L. X. Benedict, E. L. Shirley, and S. G. Louie, Hybridization Effects and Metallicity in Small Radius Carbon Nanotubes, Phys. Rev. Lett. **72**, 1878 (1994).

[114] S. Azevedo, R. De Paiva, and J. Kaschny, Stability and electronic structure of $B_xN_yC_z$ nanotubes, J. Phys.: Condens. Matter **18**, 10871 (2006).

[115] H.-Y. Liu, M.-F. Lin, and J.-Y. Wu, Essential electronic properties of silicon nanotubes, Nanomaterials **11**, 2475 (2021).

[116] B. A. Lippmann and J. Schwinger, Variational Principles for Scattering Processes. I, Phys. Rev. **79**, 469 (1950).

[117] L. P. Kadanoff and G. Baym, Conservation laws and correlation functions, Phys. Rev. **124**, 670 (1961).
[118] L. V. Keldysh, Diagram Technique for Nonequilibrium Processes, Zh. Eksp. Teor. Fiz. **47**, 1515 (1964)[Sov. Phys. JETP **20**, 1018 (1965)].
[119] D. C. Langreth, Friedel sum rule for anderson's model of localized impurity states, Phys. Rev. **150**, 516 (1966).
[120] H. U. Baranger and A. D. Stone, Electrical linear-response theory in an arbitrary magnetic field: A new Fermi-surface formation, Phys. Rev. B **40**, 8169 (1989).
[121] S. Hershfield, J. H. Davies, and J. W. Wilkins, Probing the Kondo Resonance by Resonant Tunneling Through an Anderson Impurity, Phys. Rev. Lett. **67**, 3720 (1991).
[122] Y. Meir and N. S. Wingreen, Landauer Formula for the Current Through an Interacting Electron Region, Phys. Rev. Lett. **68**, 2512 (1992).
[123] J. W. Wilkins, S. Hershfield, J. H. Davies, P. Hyldgaard, and C. J. Stanton, Noise as a diagnostic of tunneling mechanisms, Phys. Scr. **1992**, 115 (1992).
[124] P. Hyldgaard, S. Hershfield, J. H. Davies, and J. W. Wilkins, Resonant-tunneling with an electron-phonon interaction, Ann. Phys. **236**, 1 (1994).
[125] N. D. Lang, Resistance of atomic wires, Phys. Rev. B **52**, 5335 (1995).
[126] M. D. Ventra, S. T. Pantalides, and N. D. Lang, First-Principles Calculation of Transport Properties of a Molecular Device, Phys. Rev. Lett. **84**, 979 (2000).
[127] M. D. Ventra and N. D. Lang, Transport in nanoscale conductors from first principles, Phys. Rev. B **65**, 045402 (2001).
[128] G. Stefanucci and C. O. Almbladh, Time-dependent partition-free approach in resonant tunneling systems, Phys. Rev. B **69**, 195318 (2004).
[129] P. Hyldgaard, Density-functional theory of nonequilibrium tunneling, Phys. Rev. B **78**, 165109 (2008).
[130] P. Hyldgaard, Nonequilibrium thermodynamics of interacting tunneling transport: variational grand potential, density functional formulation and nature of steady-state forces, J. Phys.: Condens. Matter **24**, 424219 (2012).
[131] C. Verdozzi, G. Stefanucci, and C. O. Almbladh, Classical Nuclear Motion in Quantum Transport, Phys. Rev. Lett. **97**, 046603 (2006).
[132] N. D. Mermin, Thermal Properties of the Inhomogeneous Electron Gas, Phys. Rev. **137**, A1441 (1965).
[133] P. Hyldgaard and M. Persson, Long-ranged adsorbate-adsorbate interactions mediated by a surface-state band, J. Phys.: Condens. Matter **12**, L13 (2000).
[134] J. Repp, F. Moresco, G. Meyer, K. H. Rieder, P. Hyldgaard, and M. Persson, Substrate Mediated Long-Range Oscillatory Interaction between Adatoms: Cu /Cu(111), Phys. Rev. Lett. **85**, 2981 (2000).
[135] M. Brandbyge, P. O. J. L. Mozos, J. Taylor, and K. Stokbro, Density-functional method for nonequilibrium electron transport, Phys. Rev. B **65**, 165401 (2002).
[136] A. Minnich, M. S. Dresselhaus, Z. Ren, and G. Chen, Bulk nanostructured thermoelectric materials: current research and future prospects, Energy Environ. Sci. **2**, 466 (2009).
[137] N. T. Hung, A. R. T. Nugraha, and R. Saito, Thermoelectric properties of carbon nanotubes, Energies **12**, 4561 (2019).